Performance Analysis of a Cardiac Assist Device in Counterpulsation

N. C. Chesler

R. D. Kamm

Department of Mechanical Engineering,
Massachusetts Institute of Technology,
Cambridge, MA 02139

Performance of a cardiac assist device pumping chamber in counterpulsation was evaluated using numerical simulations of the unsteady, three-dimensional flow inside the chamber and an analytical model of the force required to eject and fill the chamber. The wall shear stress within the device was similarly computed and modeled. The analytical model was scaled to match the numerical results and then used to predict performance at physiological operating conditions. According to these models for a stroke volume of 70 ml, between 0.4 and 1.0 W is required for counterpulsation at a frequency of 1.33 Hz against a restorative spring, depending on the spring constant chosen. The power and the maximum force calculated are within the ranges a trained skeletal muscle is capable of providing. Shear stress predictions show that platelet activation in the absence of surface effects and hemolysis due to high shear are unlikely to occur with this design. Furthermore, vortices that develop in the chamber during filling are predicted to increase blood mixing and provide favorable washing of the chamber walls. A computational–analytical approach such as this may have potential to aid rapid performance evaluation of new devices and streamline the design optimization process.

1 Introduction

Approximately 2.3 million Americans suffer from chronic heart failure with 250,000 new patients diagnosed each year. It is estimated that 30,000 of these are potential candidates for the some 2000 hearts available for transplant. Because the supply of hearts suitable for transplant nationwide is unlikely to increase to meet this demand, the focus has turned to alternatives such as mechanical cardiac assist devices. An optimal cardiac assist device for permanent or very-long-term implantation has yet to be devised. An attractive power source for such a device is the body's own skeletal muscle. The use of autologous skeletal muscle to augment heart function either by cardiomyoplasty or with a skeletal-muscle ventricle (SMV) has several attractive features. These include an inherent donor source, elimination of the need for immunosuppression therapy, and the wholly internal nature of the power supply.

A hybrid muscle-powered mechanical assist device was devised, based heavily on successful SMV and mechanical assist device designs (Chesler, 1996). Following the work of Farrar et al. (1992, 1994, 1995), the chamber is artificial and mechanical whereas the power source is biological and muscular. However, this device is intended to operate in counterpulsation, much like an intra-aortic balloon pump, in contrast to the more traditional left ventricular assist device envisaged by Farrar and Hill (1992). With a counterpulsation device, the native heart is required to perform useful circulatory work, aided by the work of a skeletal muscle. Thus, the power required of the skeletal muscle in this system is less than in conventional left ventricular assist devices. Counterpulsation devices augment diastolic coronary flow by increasing diastolic pressure and decrease the work required of the native heart by decreasing systolic afterload. They also increase pressures and flow systemically. This particular design has a single inlet/outlet and therefore has no artificial valves to direct flow, but does require an intact aortic valve to prevent aortic regurgitation. The inlet/outlet enters tangential to the disklike pumping chamber to maximize swirling flows which wash the chamber walls with each cycle and increase mixing. The mechanical chamber is shown in Fig. 1, discretized into spectral elements.

Clinically, it is important to predict the force required for assist device operation when skeletal muscle is used to operate the device or when heat dissipation from a nonbiological power source is an issue. Muscular fatigue failure can be prevented if the time-varying load on the muscle can be properly designed. The clinical relevance of low shear stress is that it might be indicative of fluid stagnation and point to areas of poor mixing. Very high shear stresses in combination with long blood cell residence times are associated with the risk of platelet activation and hemolysis in bulk flow (Hellums, 1994).

Flow studies are most often used to evaluate novel assist device designs in industry (Araki et al., 1993, 1994; Kerrigan et al., 1993; McCarthy, 1995). However, these require new physical prototypes for each significant design change. These prototypes must be instrumented for pressure and/or shear stress measurements and made translucent for flow visualization. The advantages of a numerical approach to device performance evaluation are severalfold: a wide range of operating conditions can be explored, optimization of performance based on a parametric study does not require new prototype construction, and more information is obtained computationally than can be obtained experimentally, even with modern, sophisticated flow visualization techniques. The disadvantages of the computational approach are that accurate simulations of flow at physiological operating conditions require an enormous degree of resolution, computational time and memory. Also, they must be validated with experiments.

In this paper, a method to evaluate cardiac assist device performance will be presented based on numerical simulations of flow in a novel cardiac assist device, operating within a laminar regime, in combination with a scaling analysis used to predict performance at physiological operating conditions. The scaling analysis is inherently approximate, but useful information can be gained at virtually no computational cost.

Contributed by the Bioengineering Division for publication in the JOURNAL OF BIOMECHANICAL ENGINEERING. Manuscript received by the Bioengineering Division May 14, 1997; revised manuscript received January 20, 1998. Associate Technical Editor: V. T. Turitto.

 Copyright © 1998 by ASME

Downloaded 16 Mar 2009 to 128.104.192.14. Redistribution subject to ASME license or copyright; see http://www.asme.org/terms/Terms_Use.cfm

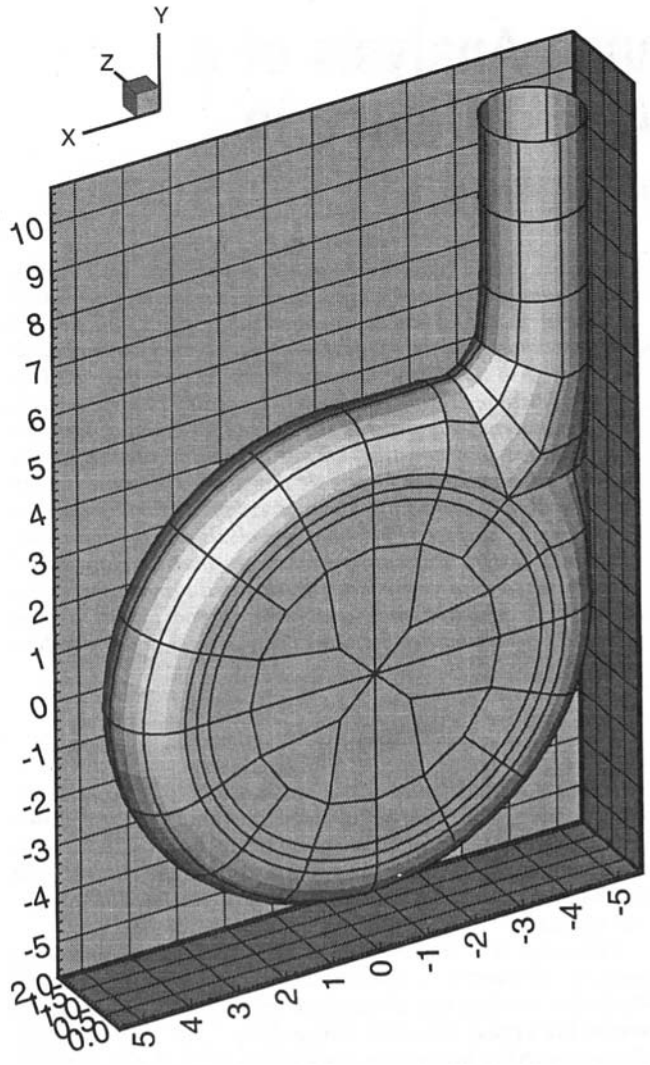

Fig. 1 Valveless mechanical pumping chamber design; dimensions in cm

2 Numerical Simulations

Numerical simulations of the unsteady, three-dimensional flow inside the pumping chamber were conducted to detail the fluid pressures, velocities and shear generated during pulsatile pumping. Operating conditions for the device *in vivo* based on a maximum stroke volume of 70 ml are shown in the first column of Table 1. The first three rows of the second column give one combination of physical parameters, which lead to the numerical, dimensionless operating conditions given in the last two rows. Geometric similarity was maintained between the two cases; dynamic similarity could not be maintained without increasing the mesh resolution to an impractical degree. This particular combination of parameters was chosen to match physical experiments being conducted on a prototype in the MIT Fluid Mechanics Laboratory. Two attempts to characterize the resulting fluid dynamic dissimilarities were made: first, by simulating flow at even higher fluid viscosity (thus lower Re and α) and then analyzing the differences between these two conditions (see Chesler, 1996), and second, by creating an analytical scaling model of the device that matches both the low and high Re simulation data and subsequently using this to predict flow characteristics at higher, more physiological operating conditions. The latter approach will be discussed at length in Section 3.

Table 1 Fluid properties and device operating conditions physiologically and in numerical simulations

	Physiological	Numerical
Density (g/cm^3)	1.07	1.07
Viscosity (g/cm s)	0.04	1.0
Frequency (Hz)	1.33	0.75
Reynolds No. (Re_h)	1600	36
Womersley No. (α)	29	4.3

The fluid dynamics in this pumping chamber design are unique and affect pumping efficiency. The impact of these flow dynamics on the potential thrombogenicity of the chamber are similarly important. In the following subsections, basic features of the simulation are presented followed by discussions of the calculated forces required for pumping, shear stress in the chamber and fluid vortices that develop.

2.1 Method. The numerical solution of the Navier–Stokes equations for flow inside the pumping chamber was carried out with the spectral element method. A commercial computational fluid dynamics (CFD) package was used (NEKTON). The spectral element technique is an efficient finite element method that offers high-order convergence and geometric flexibility. The computational domain is discretized into a series of hexahedral elements. Within each element, a local Cartesian mesh is constructed corresponding to a series of $n \times n \times n$ tensor-product Gauss–Lobatto–Legendre collocation points (that is, $(n-1)$th order polynomial interpolants are used for the velocities; the pressure has a lower order of interpolation). An arbitrary Lagrange–Eulerian description of the time-dependent domain is used to incorporate the effect of the moving boundary while an elliptic mesh solver obtains the mesh velocity and displacement at all interior nodal points (Maday and Patera, 1989; Ho and Patera, 1990; Patera, 1992, 1994).

The device geometry (10 cm diameter and 2 cm deep chamber, 2 cm diameter and 10 cm long outflow tube in this case) was discretized into 396 elements using sixth-order interpolants.

Nomenclature

d = outlet tube diameter
f = pumping frequency
F = force
h_0 = initial separation between plate and far wall; also outlet diameter
h = time-varying separation between plate and far wall
L = equivalent outflow length
P = pressure
P_a = time-varying aortic pressure
P_J = time-varying pressure at the junction of the chamber and inlet/outlet
Q = time-varying flow rate
$Q_{\max}$ = maximum flow rate
R = plate radius
U = time-varying velocity of plate
u, v_r = fluid velocities in the axial (x) and radial (r) directions, respectively
δ = boundary layer thickness
μ = fluid viscosity
ρ = fluid density
τ = shear stress
ν = dynamic viscosity
$\mathrm{Re}_h = (\rho U_{\max} h_0/\mu)$ = average Reynolds number
$\alpha = h_0\sqrt{2\pi f/\nu}$ = average Womersley number
$\widetilde{\mathrm{Re}}_h = (\rho U h_0/\mu)$ = time-varying Re_h
$\widetilde{\alpha^2} = (\rho h_0^2/\mu U)(dU/dt)$ = time-varying α

Downloaded 16 Mar 2009 to 128.104.192.14. Redistribution subject to ASME license or copyright; see http://www.asme.org/terms/Terms_Use.cfm

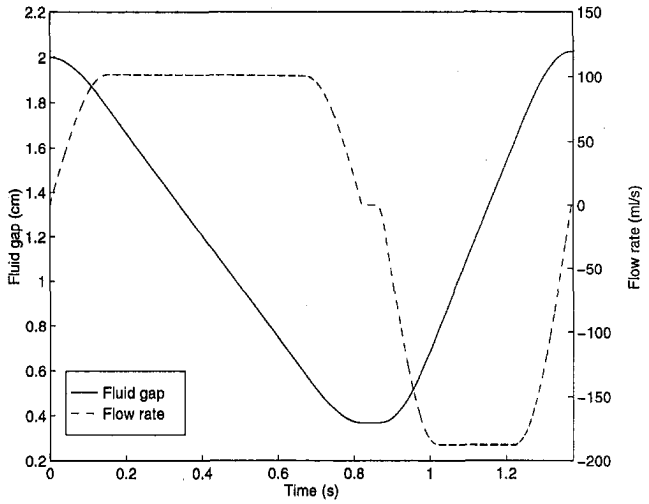

Fig. 2 Dimensional pusher plate position and resulting flow rate versus time, showing ejection followed by filling (f = 0.75 Hz)

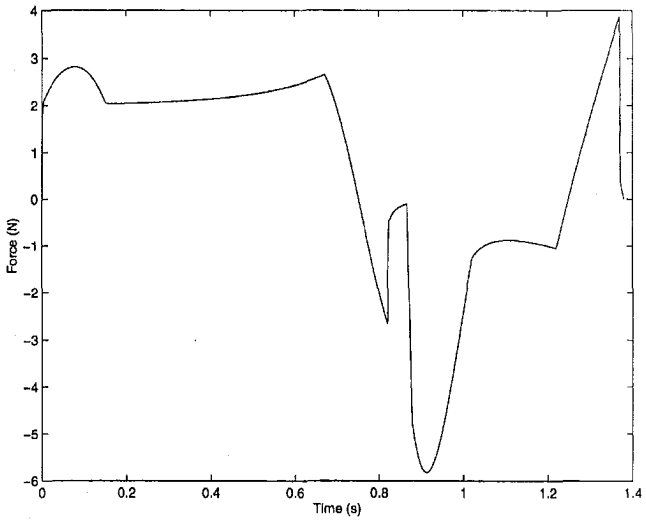

Fig. 3 Computed dimensional pusher plate force versus time

Flow was generated by imposing a moving boundary at the pusher plate, which provided oscillatory flow ranging from +100 to −200 cm^3/s. The flat, central piston and rigid side walls were joined by a ring whose deformation in the axial direction (of the chamber) varied sinusoidally with the radius. The inlet/outlet had an "outflow normal" boundary condition, which imposed normal outflow and inflow. All other boundaries were rigid walls. In order to model counterpulsation, the pusher plate moved slowly during ejection and more quickly during filling at nearly constant velocity; since filling is to occur during cardiac systole, which is roughly half the length of diastole, the filling phase of the cycle is shorter than ejection. The depth of the gap under the pusher plate, or fluid gap between the pusher plate and the far wall, versus time and resulting flow rate are shown in Fig. 2.

The accuracy of the code's three-dimensional steady solver was ascertained by simulating entrance flow in a straight tube and comparing the results with experiment. Less than 2 percent error between computed and experimental entrance lengths was found, and similar agreement was found for the development of axial velocities at seven tube radii (Chesler, 1996). He and Ku (1994) validated the two-dimensional unsteady solver with axisymmetric Womersley flow. Mesh independence of the three-dimensional, unsteady chamber simulation was measured in two ways. First, a root mean square error in mass conservation between the plate and the outlet, which was observed in lower resolution simulations (using fourth-order interpolants) for identical conditions, was reduced to less than 1 percent. Second, the isocontours of pressure were observed to be continuous at element boundaries. In the spectral element formulation, discontinuities in pressure contours, which are computed at a lower order than velocities, are a sensitive measure of the residual.

One complete cycle of ejection and filling was run at these conditions. Thus, these data represent only the fluid dynamics of device startup, not stable operating conditions for periodic pumping. Total time for these calculations on a DEC Alpha 400 was on the order of 780 hours.

2.2 Results. The force required to drive ejection and filling of the chamber was calculated by integrating the pressure forces on the plate at each time step. The plate is defined as all moving boundaries: the central rigid piston and outer deforming ring. This force is plotted versus time in Fig. 3. While only one cycle of ejection and filling was computed, axisymmetric simulations of the chamber (not presented) showed few differences between the first cycle and the second.

A contour map of the pressure on the walls of the device at one stage of ejection is shown in Fig. 4; a map of the wall shear stresses at this time is shown in Fig. 5. Note, in interpreting the pressure and shear, that the physiological Reynolds number was lowered (approximately 50-fold) for the numerical simulation and that in calculating the shear stress here it was assumed that this was due to a higher fluid viscosity. With physiological blood viscosity, the shear stress and pressure would be decreased.

Throughout filling at these operating conditions (Re_h = 36, α = 4.3), a large vortex appears in the center of the chamber while a second, smaller counterrotating vortex develops at the later stages of filling. Figure 6 shows the swirl in the chamber near the end of filling by plotting planar streamlines atop speed contours in one chamber cross section. Vortices similar to those found in curved tubes occur in the chamber annulus during both

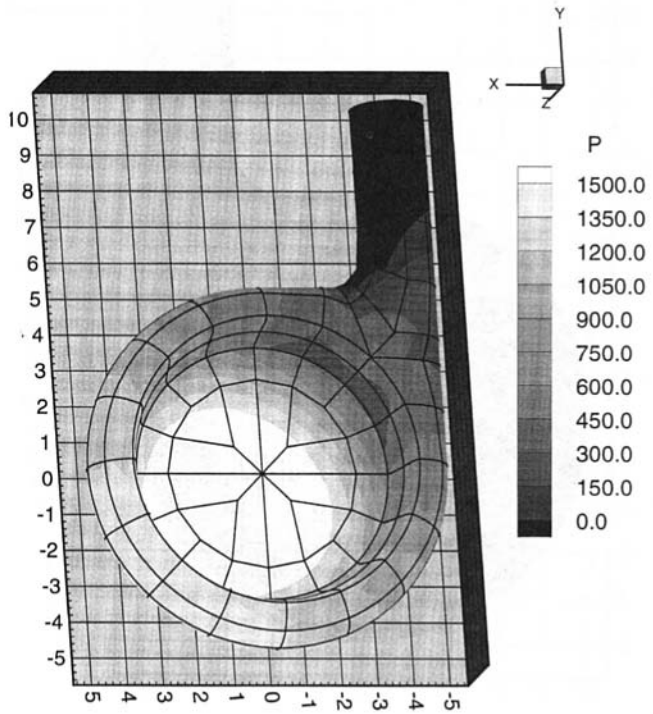

Fig. 4 Dimensional pressure contours during ejection (t = 0.73 s); axis dimensions in centimeters, pressure in dynes/cm^2

Downloaded 16 Mar 2009 to 128.104.192.14. Redistribution subject to ASME license or copyright; see http://www.asme.org/terms/Terms_Use.cfm

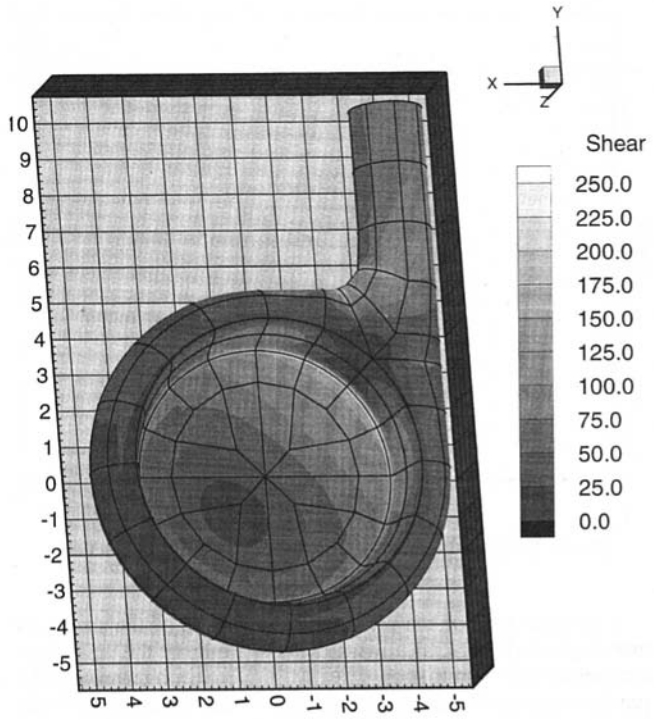

Fig. 5 Dimensional shear stress contours during ejection (t = 0.73 s); axis dimensions in centimeters, shear stress in dynes/cm^2

filling and ejection as shown on the left in Fig. 7. During ejection, these secondary vortices extend into the straight outlet tube whereas during filling, inflow is parallel to the tube walls and no secondary flows develop. Note that while secondary

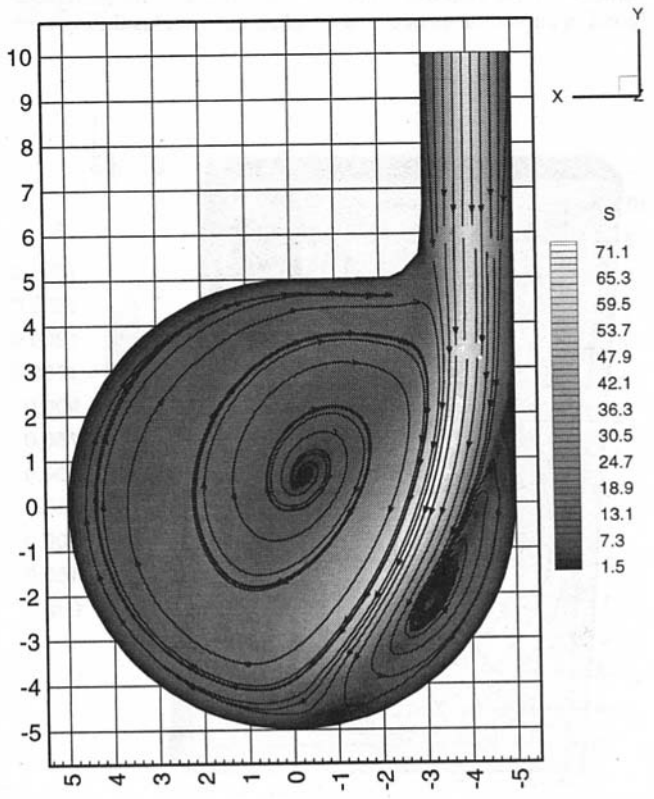

Fig. 6 Swirl in the chamber centerplane near the end of filling shown by plotting streamlines atop speed contours (t = 1.3 s); speed in cm/s

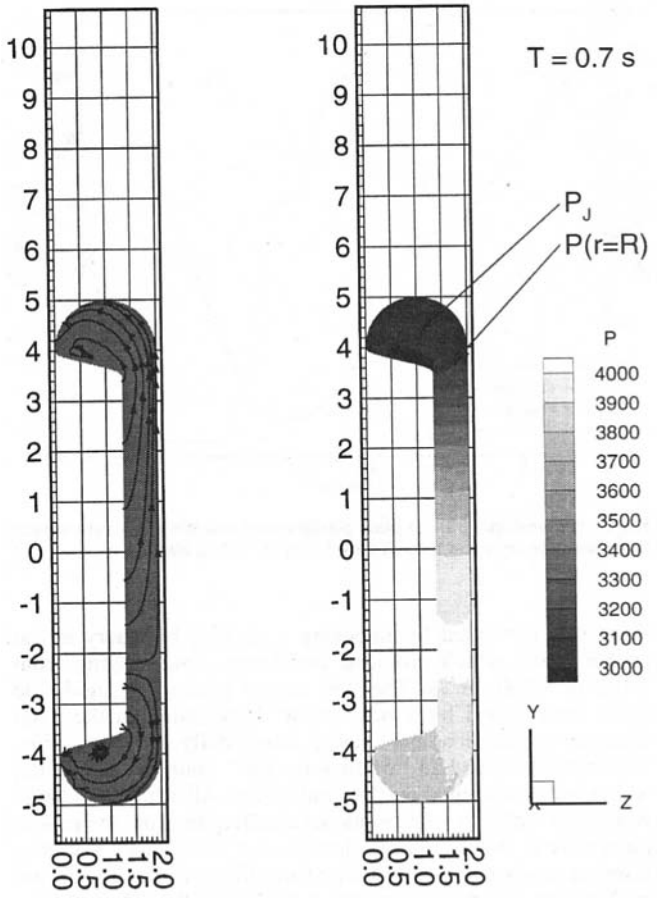

Fig. 7 Streamlines (left) and dimensional pressure distribution (right) beneath the plate (y = 0) during ejection (t = 0.7 s, units of pressure dynes/cm^2, dimensions in cm)

vortices in the outlet tube are evident during ejection, precise computation of their decay characteristics (length, for example) in the outlet may not be reliable since the outflow boundary condition may influence the upstream fluid dynamics.

2.3 Discussion of Numerical Results. The force required to drive ejection and filling is sensitive to plate acceleration and deceleration; the fluctuations at the beginning of ejection, plate reversal, and end-filling are quite large. In contrast, the force is nearly constant when the flow rate is constant (during mid-ejection, briefly in-between ejection and filling, and then during mid-filling), except near the end of ejection when the required force increases slightly. This rise is likely due to the increased shear under the plate as the fluid gap decreases. Given that the effects of temporal acceleration and shear are discernible in the force plot, we can infer that both temporal acceleration and viscous stresses are important to the chamber fluid dynamics. However, detecting the influence of convection and determining the relative importance of temporal, convective, and viscous effects are not as straightforward. Furthermore, predicting quantitatively how these features and their relative influence would change at physiological conditions may be impossible with these data alone. The scaling model presented in Section 3 will address both of these issues.

It was observed in shear contour plots at various times during ejection (but not shown here) that very low shear stress regions occur during pumping but migrate from one section of the chamber to another. The highest shear stresses in the chamber at all times during the cycle occur at the edge of the pusher plate. As fluid flows from between the plates into the annular region, it separates in a manner similar to that seen in flow over a back-

Downloaded 16 Mar 2009 to 128.104.192.14. Redistribution subject to ASME license or copyright; see http://www.asme.org/terms/Terms_Use.cfm

ward-facing step. A peak in shear occurs on the rigid portion of the piston just before the point of flow separation. The next highest stresses occur in the inlet/outlet. The surface area subject to high shear in the outlet is much larger than the area subjected to high shear at the boundary of the pusher plate, however. Thus, the residence time of blood particles in the outlet will be longer than at the edge of the pusher plate and may have more effect on blood cell activation and damage.

The fluid vortices that occur are also relevant to device performance. The risk of blood coagulation due to fixed recirculation zones and fluid stagnation can be assessed qualitatively in this way. With this design, the large central vortex will wash the walls and should prevent stagnation. At physiological conditions, the momentum of the inflow jet would increase, further amplifying the swirl in the chamber. The combination of the central and annular vortices should prevent stationary recirculation zones or unmixed, stagnant pools of blood.

3 Scaling Analysis

These numerical simulations provide detailed flow information at every time step for various flow conditions (Re_h or α) but it is not obvious how these fluid dynamics will change at physiological operating conditions (which are beyond present computational capabilities of NEKTON and other spectral element codes). This section presents a simple model of flow in the outlet tube and beneath the pusher plate, which is shown to be consistent with the more detailed computations for one set of parameters. The model and parameters are then used to predict pumping chamber performance at physiological Reynolds and Womersley numbers.

3.1 Model Development. We are interested in a simple model of the forces required to operate the counterpulsating pump. The force is determined by the pressure distribution beneath the pusher plate and the pressure drop in the annulus and outlet. For the purpose of obtaining scaling relationships, we treat flow in the inlet/outlet as fully developed and undirectional, and flow beneath the pusher plate as axisymmetric. In the outlet tube under these conditions, the Navier–Stokes equation can be written:

$$\frac{\partial P}{\partial x} \cong \mu \frac{1}{r}\frac{\partial}{\partial r}\left(r\frac{\partial u}{\partial r}\right) - \rho\left(\frac{\partial u}{\partial t} + u\frac{\partial u}{\partial x}\right), \qquad (1)$$

where the fluid viscosity multiplies the viscous term, and the density multiplies the temporal and convective acceleration terms, in that order. The flow rate in the outlet tube (of diameter h_0) is Q and the pressure at the outlet boundary is taken to be a reference value, zero. The total pressure drop in the annulus and outlet can be represented by a Poiseuille pressure drop in a straight tube of length L. Then, the pressure at a point just inside the pumping chamber, in the annulus, where the flow channel has expanded and the velocity has fallen can be approximated as

$$P_J \cong \frac{128\mu QL}{\pi h_0^4} + \rho\left(\frac{4}{\pi h_0^2}\frac{dQ}{dt}L + \frac{1}{2}\left(\frac{4}{\pi h_0^2}Q\right)^2\right) \qquad (2)$$

using a parabolic axial flow profile to estimate the viscous term (that multiplied by the viscosity). Again, the temporal and convective terms are those multiplied by the fluid density where the temporal is the first—proportional to the time derivative of Q—and the convective is the second—proportional to Q^2. The assumption of parabolic flow will be discussed in the following section. At these operating conditions, the unsteady term is the largest contributor to the total force required to drive the plate, all but overwhelming the viscous and convective inertia contributions.

Beneath the pusher plate, we approximate the flow by an axisymmetric radial flow. When the fluid gap becomes small and this contribution is most important, the radial component of the Navier–Stokes equation simplifies to

$$\rho\left(\frac{\partial \nu_r}{\partial t} + \nu_r\frac{\partial \nu_r}{\partial r}\right) \cong -\frac{\partial P}{\partial r} + \mu\frac{\partial^2 \nu_r}{\partial x^2}. \qquad (3)$$

Again assuming a parabolic flow profile and given the following expression for mass conservation (for $0 \le r \le R$)

$$Q(r, t)_{\text{plate}} = U\pi r^2 = 2\pi r\bar{\nu}_r(h_0 - Ut), \qquad (4)$$

we can approximate the pressure gradient as

$$\frac{\partial P}{\partial r} \cong -\frac{6\mu\bar{\nu}_r}{(h_0 - Ut)^2} - \rho\left(\frac{d\bar{\nu}_r}{dt} + \frac{1}{2}\frac{\overline{d(\nu_r)^2}}{dr}\right)$$

$$= -r\left(\frac{3\mu U}{h^3} + \frac{\rho}{2}\frac{d(U/h)}{dt} + \frac{\rho}{4}\frac{U^2}{h^2}\right) \qquad (5)$$

defining the time-varying separation between the plate and chamber far wall as $h = h_0 - Ut$. Integrating from an arbitrary radial location r to the edge of the plate, we have

$$P(r) - P_J \cong \frac{1}{2}(R^2 - r^2)\left(\frac{3\mu U}{h^3} + \frac{\rho}{2}\frac{d(U/h)}{dt} + \frac{\rho}{4}\frac{U^2}{h^2}\right)$$

$$= \frac{1}{2}(R^2 - r^2)\left(\frac{3\mu U}{h^3} + \frac{\rho}{2}\frac{1}{h}\frac{dU}{dt} + \frac{3}{4}\frac{\rho U^2}{h^2}\right). \qquad (6)$$

Here, we have let the pressure at the edge of the plate at $r = R$ be equal to P_J, the pressure in the annulus near the outlet. The computational results support this approximation; a representative example of the pressure distribution from the center of the plate to the annulus is given on the right in Fig. 7. This figure also demonstrates the lack of axisymmetry under the plate in the full simulation; note however that symmetry about a diagonal through the chamber does exist, as shown in Figs. 4 and 5.

Finally, the force required to displace the pusher plate is the integral of the plate pressure distribution over the pusher plate area. Dimensionlessly, that is,

$$\frac{F}{\mu Q_{\max}R^2/h_0^3} \cong \frac{Q}{Q_{\max}}\left[\left(\frac{128L}{h_0} + \frac{3h_0^3}{4h^3}\right)\right.$$

$$\left. + \widetilde{\mathrm{Re}}_h\left(\frac{8R^2}{h_0^2} + \frac{3h_0^2}{16h^2}\right) + \widetilde{\alpha^2}\left(\frac{4L}{h_0} + \frac{h_0}{8h}\right)\right] \qquad (7)$$

where $\widetilde{\mathrm{Re}}_h = (\rho U h_0/\mu)$ and $\widetilde{\alpha^2} = (\rho h_0^2/\mu U)(dU/dt)$ are taken to be time-varying, contrary to conventional usage. Given Q, $Q_{\max}$, h_0, R and the fluid properties, this approximate analytical expression for the pusher plate force can be plotted versus time, for some equivalent outflow length, L chosen to best fit the numerical data.

3.2 Model Validation. Figure 8 plots force versus time obtained by the numerical simulation and computed from Eq. (7) for $(L/h_0) = 7$. Force is nondimensionalized as in Eq. (7) above and time is nondimensionalized by the pumping frequency, f. The flow rate in the model, Q, is set equal to the flow rate from the simulation; the pusher plate velocity and acceleration were then back-calculated from the outlet flow rate and plate area.

Several features of the force required over time are captured by the model: the early peak in force during plate acceleration,

Downloaded 16 Mar 2009 to 128.104.192.14. Redistribution subject to ASME license or copyright; see http://www.asme.org/terms/Terms_Use.cfm

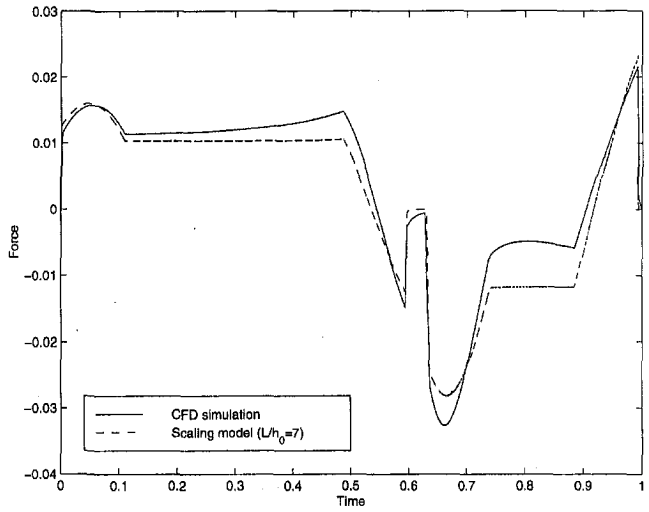

Fig. 8 Dimensionless pusher plate force versus time for numerical simulation and model; $L/h_0 = 7$

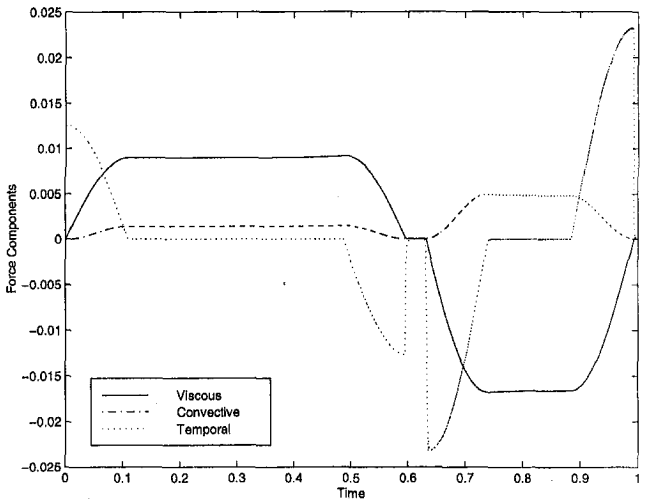

Fig. 9 Dimensionless viscous, inertial and unsteady components of the model force, $L/h_0 = 7$

the oscillation near flow reversal, the substantial negative peak in force during early filling, and the sharp peak in force at the end of the cycle. The various components of Eq. (7) for these flow conditions are plotted separately in Fig. 9: the quasi-steady viscous, convective, and temporal acceleration terms. Notice that the temporal acceleration term is discontinuous where the change in flow rate is discontinuous (that is, where dQ/dt is discontinuous); it is zero when dQ/dt is zero.

Two features of the computational force plot are not well captured by the single-parameter model: the slow rise in force near the end of ejection and the degree of pressure recovery during filling. However, in view of the fact that the model was developed with scaling arguments, we can justifiably add auxiliary constants into the model to achieve a better fit with the data. That is, we can rewrite Eq. (7) as

$$\frac{F}{\mu Q_{\max} R^2/h_0^3} = \frac{Q}{Q_{\max}}\left[c_1\left(\frac{128L}{h_0} + c_2\frac{3h_0^3}{4h^3}\right)\right.$$

$$\left. + c_3\,\widetilde{\mathrm{Re}}_h\left(\frac{8R^2}{h_0^2} + c_4\frac{3h_0^2}{16h^2}\right) + c_5\tilde{\alpha}^2\left(\frac{4L}{h_0} + c_6\frac{h_0}{8h}\right)\right] \quad (8)$$

and then test c_i until a best fit is obtained. Using least squares to assess the best fit for $0.1 \le c_i \le 10$, $c = (0.96, 7.40, 2.24, 2.09, 0.87, 14.66)$ yields the curve shown in Fig. 10.

Both the original and modified scaling arguments provide physical insight that is not obvious from the CFD calculation. If, for the conditions imposed in the numerical simulation, c_1 and c_2 were both approximately one, we could infer that flow under the plate and flow in the outlet were predominantly parabolic. If c_2 were order one and c_1 greater, we could infer that neither is parabolic, but both have similar boundary layer thickness, determined by either temporal or spatial accelerations. However, since c_2 is significantly greater than one (and c_1 is not), the shear stresses beneath the plate and in the outlet tube appear to have been influenced to different degrees by these effects, at these operating conditions. That is, we could predict that flow in the outlet tube is nearly parabolic, whereas under the plate it is not. Observation of the numerically computed velocity profiles in these locations verifies this prediction: In the outlet, the profiles are blunted parabolas, whereas under the plate, the profiles show substantial reversal in the core and have steep gradients near both the top and bottom walls more typical of Womersley flow.

The constants c_3, c_4, and c_6 are approximately 2-, 2-, and 15-fold greater than one, respectively. These are the modifiers of the total convective inertia term (under the plate and in the outlet), the convective inertia term under the plate and the temporal inertia term under the plate. Two assumptions made in the scaling model likely contribute to the underestimation of the force contribution from convective acceleration: the lack of axisymmetry in flow under the plate, and the nonuniform velocity profiles under the plate and in the tube. As the shear contours in Fig. 5 demonstrate, much of the flow under the plate, especially that farthest from the outlet, is traveling both farther and faster than would be required for axisymmetric flow. Thus the pressure gradient required to accelerate the flow is higher than would be predicted in an axisymmetric case. Also, by assuming symmetric flow, the model cannot account for vortical flow either under the plate (during filling) or in the outlet tube (during ejection). Since the energy required to both form and dissipate these structures is not accounted for, we would predict that the model would underestimate the total force, which is indeed the case.

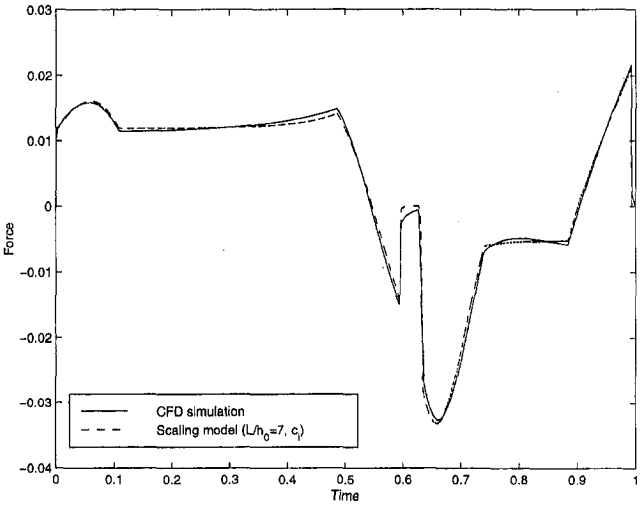

Fig. 10 Dimensionless pusher plate force versus time for numerical simulation and six-parameter model; $L/h_0 = 7$; c = (0.96, 7.40, 2.24, 2.09, 0.87, 14.66)

Downloaded 16 Mar 2009 to 128.104.192.14. Redistribution subject to ASME license or copyright; see http://www.asme.org/terms/Terms_Use.cfm

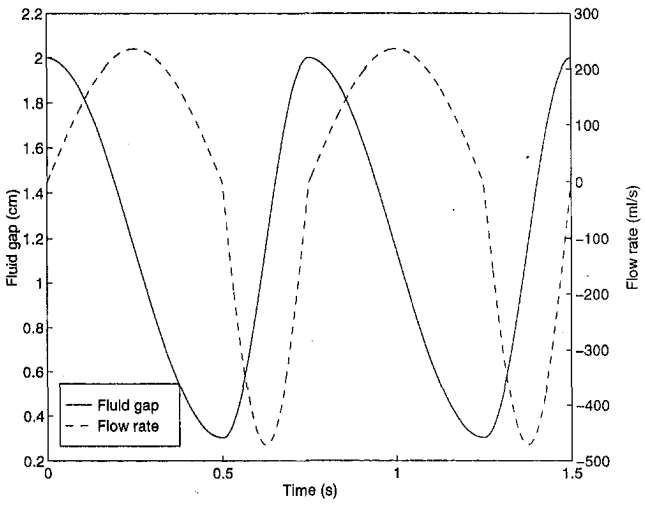

Fig. 11 Dimensional plate displacement and resulting flow rate versus time for two cycles (heart rate = 80 bpm or f = 1.33 Hz)

Second, uniform velocity profiles were used to estimate the momentum of flow. In fact, parabolic flow requires 1.2 times more momentum to accelerate than uniform flow in a two-dimensional channel and 1.33 times more in a tube. It would be difficult to calculate the scale factor for the nonuniform, nonparabolic profiles generated here but using uniform flow profiles is certainly an underestimation.

The lack of flow axisymmetry under the plate is also likely to be the reason for the rather large magnitude of the sixth constant in Eq. (8). The velocity profiles will not affect the pressure gradient required to accelerate the flow temporally, but the length over which that acceleration takes place will. Since much of the flow under the plate is traveling farther than the characteristic plate radius R, and must travel at a higher velocity than in an axisymmetric flow, more pressure and thus force will be required to overcome its inertia. Also, the time-dependent nature of the vortices during filling will contribute to temporal accelerations in the flow.

While it is not surprising that the coefficients take on values different from unity, the significant deviations of c_2 and c_6 are larger than one would expect and difficult to justify. It should be noted, however, that the contributions to the total force of those terms associated with plate effects are, in general, quite small. For example, setting c_6 to one produces a significant effect only during the interval t = 0.63 to 0.7 (flow reversal) and setting c_2 to one is primarily noticeable when t = 0.4 to 0.5 (end ejection). It might therefore be expected that the uncertainty in estimating the coefficients corresponding to plate effects (c_2, c_4 and c_6) will be large.

3.3 Model Predictions Under Physiologic Conditions. Given the observation that the pusher plate force is sensitive to discontinuities in plate acceleration and deceleration, a smoother plate velocity function was specified for operation at physiological conditions (see Table 1 for parameter values). To undergo a smooth transition from a slow ejection to a rapid filling cycle, two sine waves were juxtaposed: one with a frequency $2/3f$, the other with a frequency $1/3f$. A physiological heart rate of 80 bpm (f = 1.33 Hz) was chosen, and the stroke volume was maintained at 70 ml. Figure 11 shows two cycles of this plate displacement (or fluid gap) versus time and the resulting flow rate. In this case, dQ/dt is discontinuous at only two points in the cycle (instead of four) and is equal to zero only twice (at mid-ejection and mid-filling).

3.3.1 Force and Shear Stress. At these new operating conditions, some assumptions made in the scaling model of the counterpulsation device obviously fail. In particular, the first two terms in Eq. (7) were obtained by assuming that the velocity profiles in the outlet and under the plate (respectively) were parabolic. As the discussion of auxiliary constants above demonstrated, this assumption failed even at low-frequency operation.

These shear components of the force should scale with the viscosity of the fluid, the velocity of flow in the flow direction, and inversely with the thickness of the boundary layer (or half the tube diameter in fully developed tube flow). In unsteady flow, the boundary layer thickness δ is approximately $3\sqrt{\nu/2\pi f}$ so that the shear stress scales as

$$\tau \approx \frac{\mu U}{\delta} \approx \frac{\alpha}{3}\frac{\mu U}{h_0}. \tag{9}$$

Or, if a Blasius boundary layer is assumed where $\delta \cong 5\sqrt{\nu L/U}$ then the shear stress can be written

$$\tau \approx \frac{1}{5}\left(\mathrm{Re}_h \frac{h_0}{L}\right)^{1/2}\frac{\mu U}{h_0}. \tag{10}$$

The effect of these stresses on the force can be estimated by scaling the first two terms in Eq. (7). Assuming first that the unsteady effects dominate both under the plate and in the outlet, both terms would be greater by a factor of approximately 10 (when the fluid gap is small). Assuming a Blasius boundary layer, both terms are amplified by roughly 4. In the worst case scenario with the highest shear forces, the total force predicted with amplified shear components as well as the temporal and convective inertial terms are shown dimensionally for two pumping cycles in Fig. 12.

If the contributions to the force from the pusher plate and the outlet tube are plotted separately, an interesting observation can be made: The sum of the viscous, convective, and temporal inertia terms in the outlet tube is two to ten times higher than that from under the plate, depending on the point in the cycle. The same holds true in the breakdown of force at simulation (nonphysiological) conditions. Rewriting Eq. (8) for an arbitrary outlet tube diameter d, we see that increasing the outlet tube area would decrease the outlet tube contribution to force, and thus significantly decrease the total force:

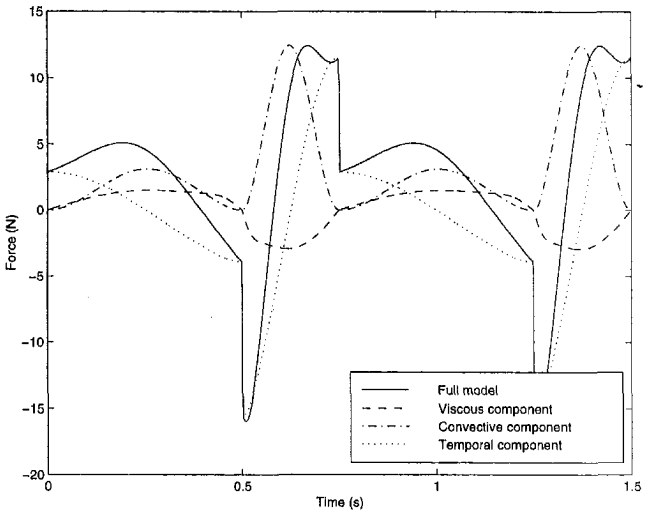

Fig. 12 Dimensional viscous, inertial and unsteady components, and total of the model force according to Eq. (8) at physiological operating conditions; L/h_0 = 7; c = (9.61, 7.40, 2.24, 2.09, 0.87, 14.66)

Downloaded 16 Mar 2009 to 128.104.192.14. Redistribution subject to ASME license or copyright; see http://www.asme.org/terms/Terms_Use.cfm

$$\frac{F}{\mu Q_{\max} R^2/h_0^3} = \frac{Q}{Q_{\max}} \left\{ c_1 \left(\frac{128L}{h_0} \frac{h_0^4}{d^4} + c_2 \frac{3h_0^3}{4h^3} \right) + c_3 \widetilde{\mathrm{Re}}_h \left(\frac{8R^2}{h_0^2} \frac{h_0^4}{d^4} + c_4 \frac{3h_0^2}{16h^2} \right) + c_5 \tilde{\alpha}^2 \left(\frac{4L}{h_0} \frac{h_0^2}{d^2} + c_6 \frac{h_0}{8h} \right) \right\} \quad (11)$$

However, this equation cannot be optimized for d, since there exists no term to limit its increase. Physically, as the outlet tube diameter increases, fluid dynamics in the junction will become more important and the two-component (chamber-tube) scaling model will fail. Also, the shear stresses in the outlet tube will fall, potentially leading to quasi-stagnant flow and thrombogenesis. A simulation at low Re and α, but with a wide outlet tube, could shed light on important details of the fluid dynamics in this region and the potential improvements in the scaling model.

3.3.2 Blood Cell Activation. Shear stress is also important in terms of its potential effect on blood cell activation. As noted earlier, a zone of maximum shear stress is observed at the outer circumference of the pusher plate. To examine this tendency further, and to verify how shear stress beneath the plate would scale with α, the larger of the effects discussed above, a simple axisymmetric simulation of chamber deformation was performed. The center of the chamber became the axis of symmetry for this model. Top and bottom walls were the far wall and pusher plate, respectively. Here, the deforming region had the same radius and pattern of deformation as the pusher plate in the full three-dimensional chamber simulation. Since the chamber outlet could not be mimicked in an axisymmetric model, the chamber annulus was extended radially, and had an outflow normal boundary condition imposed. The simulation was run for two cycles of ejection and filling with the same pusher plate displacement used in the physiological simulation; the viscosity of the fluid was changed to vary α; α = 7 and 21 were tested. The shear stress on the both flat and deforming regions of the pusher plate were observed to scale with the α during most of ejection and filling.

Assuming this relationship holds in the nonaxisymmetric chamber, peak stresses around the rim of the pusher plate would be approximately 170 dynes/cm^2 during filling (scaled according to Eq. (9) for physiological conditions). A conservative estimate of the transit time of a red cell past the narrow region of peak shear is 0.03 seconds (based on a speed of 10 cm/s and length of 0.3 cm); according to Hellums et al. (1994) data on bulk flow effects on blood cell behavior, this should not cause red blood cell hemolysis or platelet activation in the absence of surface-driven phenomena. Platelet aggregation and adhesion secondary to the material properties of the device, and sublethal damage cannot be predicted from these data.

The slower transit times through the outlet, where the shear stresses are not as high, may lead to greater *in vivo* risk of hemolysis. Again using α to scale the shear stresses calculated in the three-dimensional CFD simulation, the predicted shear is 90 dynes/cm^2 very close to the walls. The transit time through the inlet/outlet during filling is approximately 0.2 seconds, given the mean flow rate and inlet length. This shear stress exposure–residence time is equivalent to that of the microcirculation, i.e., negligible. Two qualifications must be made, however. On the one hand, in the thin boundary layer the velocities are lower than in the mean flow, so the transit times are longer. On the other, while the inflow during filling is essentially unidirectional, during outflow secondary flows exist. These secondary flows will increase mixing near the walls, thereby decreasing both transit times and shear stresses in the outlet.

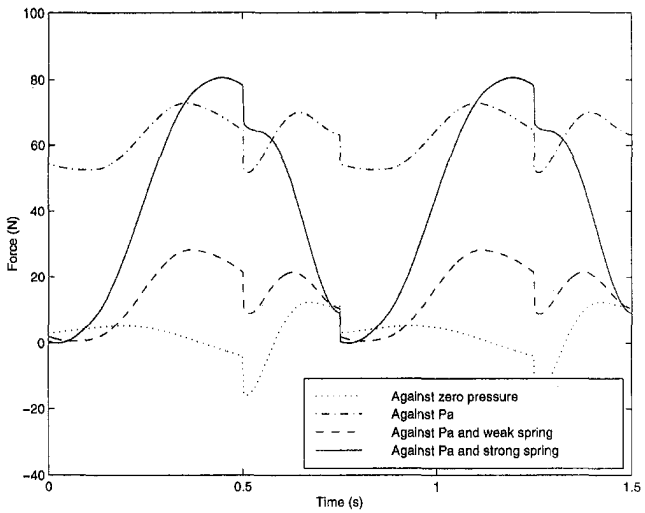

Fig. 13 Dimensional force required for two cycles of physiological operation against zero pressure (dotted line), aortic pressure (Pa, dash-dotted line) and against aortic pressure aided by a weak (dashed line, k = 5.7 dynes/cm) and strong (solid line, k = 40 dynes/cm) linear spring; L/h_0 = 7; c = (9.61, 7.40, 2.24, 2.09, 0.87, 14.66)

3.3.3 Aortic Pressure Compensation. An important clinical factor yet to be considered in the device evaluation is the time-varying aortic pressure. Given that human aortic pressure data vary, that data for the patient population at risk will vary even more, and that the device itself will change the pressure trace at the aorta, no attempt was made to model the dichrotic notch or other normal, physiological features of the aortic pressure waveform. Instead, the modified-sinusoid plate displacement profile was shifted 90 deg out of phase and used to model pressure in the aorta. In this way, the chamber ejects during systole (h is small when the pressure is high) and fills during diastole (vice versa). To compensate for the aortic mean pressure and aid filling, a linear spring can be incorporated into the device, chosen so that one muscle can supply the remaining required forces in contraction. Here we choose the spring to enable filling, whereas the stimulated-muscle contraction provides the impulse of power required for ejection. In other words, the force required of the muscle during ejection (the first 0.5 s of each cycle) must be entirely contractile; then, the spring forcibly stretches the muscle and pulls back the pusher plate during filling.

Figure 13 plots the predicted pusher plate force acting against zero pressure (dotted line), aortic pressure (dash-dotted line), and aortic pressure counteracted by a weak and strong spring with the rest length adjusted so that all of ejection requires positive force (dashed and solid lines, respectively). The strong and weak spring constants were 40 and 5.7 dynes/cm, with rest lengths −0.65 cm and 7.23 cm, respectively. Adding either spring increases the maximum force required but makes the system feasible for one skeletal muscle. At these operating conditions, the predicted maximum force and power required for the strong and weak spring configurations are 87 N and 1.0 W and 33 N and 0.4 W, respectively. Clearly, skeletal muscle work against a strong spring must be greater than against a weak spring. However, the stronger spring smoothes the force required with respect to time. This feature might eliminate inadvertent backflow or abrupt changes in flow direction that could result from power demand and supply mismatch.

Normal, healthy heart muscle supplies approximately 2 to 4 W/kg at rest, and can produce up to 16 W/kg during very heavy exercise (Salmons and Jarvis, 1990, 1992). Minimally conditioned rabbit skeletal muscle has been shown to provide 10 W/kg with a loss in power of 10 percent over 6 hours (Salmons and Jarvis, 1990); well-conditioned canine muscle

Downloaded 16 Mar 2009 to 128.104.192.14. Redistribution subject to ASME license or copyright; see http://www.asme.org/terms/Terms_Use.cfm

generated 2.6 W/kg for over nine weeks at 54 bpm with the muscle wrapped into a ventricular shape (Acker et al., 1986). The wrapped configuration accounts for a reduction in efficiency, but interspecies differences cannot be discounted. Salmons and Jarvis (1992) have estimated that a 225 g conditioned, human lattisimus dorsi muscle would be able to provide up to 1.8 W of power in the long term. This value exceeds even the estimated power requirements of our device with the stronger spring in place. However, electromechanical losses between the muscle and assist device can be assumed, suggesting an optimal spring constant between the two tested here. In addition, the peak force required by the stronger spring may be beyond the capabilities of a conditioned, human skeletal muscle. Reichenbach and Farrar (1994) found a 250 g porcine latissimus dorsi muscle capable of producing a maximum of 80 N of force in an unconditioned state, yet chronic stimulation leads to a loss of both weight and cross-sectional area, which reduces maximum muscle force (Salmons and Jarvis, 1990).

4 Conclusions

The combination of numerical simulations and an analytical model to evaluate flow in a ventricular assist device and assess its clinical potential is a novel approach to a vexing problem. Currently devices are tested by costly and time-consuming flow visualization studies, which do not yield complete information. Simulations provide detailed information at all stages of operation but can rarely be run at physiological operating conditions due to the computational memory and time requirements which were significant even at conditions used here. Approximate analytical models cannot be used without validation.

By adjusting one length parameter, an analytical model for flow in a single inlet/outlet counterpulsating cardiac assist device was a good predictor of the force required to fill and eject the chamber; a more sophisticated six-parameter model was an excellent predictor of the force obtained by numerical simulation at operating conditions $\mathrm{Re}_h = 36$ and $\alpha = 4.3$. This model was then used to predict the force and power requirements for physiological operation. Further, at high Womersley numbers, the shear stress was predicted to scale with the Womersley number (and validated numerically) enabling predictions of shear stress exposure to blood cells. The additional force required to overcome a non-zero, time-varying aortic pressure was calculated and used to test two spring constant values for a restorative spring to aid filling and offset the effect of the mean aortic pressure. The power and forces necessary to provide counterpulsatile assist against aortic pressure and an intermediate strength restorative spring (from 0.4 to 1.0 W and up to perhaps 60 N) are within the capabilities of trained skeletal muscle, even in the long term.

Flow patterns, force and power calculations were performed for one device design and one pumping pattern at physiological conditions. For this or any design, a more optimal counterpulsating, pumping pattern for use with skeletal muscle, minimizing the amplitude and duration of required force likely exists. An advantage of the approach developed here is that the dependence of required force and power on design and operational changes in the device can be seen readily. Furthermore, physical insight provided by the model can steer the designer toward improvements according to the fluid dynamics in the device or the limitations of the power source.

Acknowledgments

The authors gratefully acknowledge the support of a National Science Foundation Fellowship (to NCC) and wish to thank Dr. Matthias Heil of Cambridge University and Dr. Lee Ho of Nektonics for many helpful discussions.

References

Acker, H., Mannion, Salmons, and Stephenson, 1986, "An Autologous Biologic Pump Motor," *Journal of Thoracic and Cardiovascular Surgery,* Vol. 92(4), pp. 733–745.

Araki, K., Y. Taenaka, et al., 1993, "A Flow Visualization Study of Centrifugal Blood Pumps Developed for Long-Term Usage," *Artificial Organs,* Vol. 17(5), pp. 307–312.

Araki, K., Y. Taenaka, et al., 1994, "A Flow Visualization Study of the NCVC Centrifugal Blood Pump," *Artificial Organs,* Vol. 18(9), pp. 669–672.

Chesler, N. C., 1996, "Ventricular Assist Device Design and Analysis: A Computational Approach," Ph.D. Thesis, The Harvard Medical School—Massachusetts Institute of Technology Division of Health Sciences and Technology, Cambridge, MA.

Farrar, D., and J. Hill, 1992, "A New Skeletal Linear-Pull Energy Converter as a Power Source for Prosthetic Circulatory Support Devices," *Journal of Heart and Lung Transplant,* Vol. 11, pp. s341–50.

Farrar, D. J., S. H. Reichenbach, et al., 1994, "In Vivo Measurements of Skeletal Muscle in a Linear Configuration Powering a Hydraulically Actuated VAD," *ASAIO J.,* Vol. 40(3), pp. M309–M313.

Farrar, D. J., S. H. Reichenbach, et al., 1995, "Mechanical Advantage of Skeletal Muscle as a Cardiac Assist Power Source," *ASAIO J.,* Vol. 41(3), pp. M481–484.

He, X., and Ku, D., 1994, "Unsteady Entrance Flow Development in a Straight Tube," ASME JOURNAL OF BIOMECHANICAL ENGINEERING, Vol. 116, pp. 355–360.

Hellums, J. D., 1994, "Biorheology in Thrombosis Research," *Annals of Biomedical Engineering,* Vol. 22, pp. 445–455.

Ho, L.-W., and A. T. Patera, 1990, "A LeGendre Spectral Element Method for Simulation of Unsteady Incompressible Viscous Free-Surface Flows," *Comp. Meth. Appl. Mech. Engr.,* Vol. 80, pp. 355–366.

Kerrigan, J., F. Shaffer, et al., 1993, "Fluorescent Image Tracking Velocimetry of the Nimbus AxiPump," *ASAIO J.,* Vol. 39, pp. M639–M643.

Maday, Y., and A. P. Patera, 1989, "Spectral Element Methods for the Incompressible Navier–Stokes Equations," *State-of-the-Art Surveys on Computational Mechanics,* A. K. N. a. J. T. Oden, ed., American Society of Mechanical Engineers, pp. 71–143.

McCarthy, P. M., 1995, "HeartMate Implantable Left Ventricular Assist Device: Bridge to Transplantation and Future Applications," *Annals of Thoracic Surgery,* Vol. 59(2 Suppl), pp. S46–51.

Patera, A., 1992, *Computational (Incompressible) Fluid Dynamics: Lecture notes,* Massachusetts Institute of Technology.

Patera, A., 1994, "A Spectral Element Method for Fluid Dynamics; Laminar Flow in a Channel Expansion," *Journal of Computational Physics,* Vol. 54, p. 468.

Reichenbach, S. H., and D. J. Farrar, 1994, "Characterization and Work Optimization of Skeletal Muscle as a VAD Power Source," *ASAIO J.,* Vol. 40(3), pp. M359–M364.

Salmons, S., and J. C. Jarvis, 1990, "The Working Capacity of Skeletal Muscle Transformed for Use in a Cardiac Assist Role," *Transformed Muscle for Cardiac Assist and Repair,* R.-J. Ciu and I. Bourgeois, eds., Mount Kisco, NY, Future Publishing Company, Inc., Vol. 2, pp. 89–104.

Salmons, S., and J. C. Jarvis, 1992, "Cardiac Assistance From Skeletal Muscle: A Critical Appraisal of the Various Approaches," *British Heart Journal,* Vol. 68(3), pp. 333–338.

Downloaded 16 Mar 2009 to 128.104.192.14. Redistribution subject to ASME license or copyright; see http://www.asme.org/terms/Terms_Use.cfm